# Influence of Si Addition on the Microstructure and Mechanical Behaviour of Mg-5sn-3zn-1mn Alloy

**Sundarraju G** ( sundararajumech@gmail.com )
Kamatchi Polytechnic College https://orcid.org/0000-0003-4808-973X
**Thankathurai K.R**
Jayaram College of Engineering and Technology
**Anand Charman C**
K Ramakrishna College of Engineering

**Research Article**

**Keywords:** Magnesium, Mechanical Property, Mg-Sn alloy, Microstructure, Mg2Si.

**Posted Date:** April 12th, 2021

**DOI:** https://doi.org/10.21203/rs.3.rs-266508/v1

# Abstract

The microstructural, mechanical behaviour of Mg-5Sn-3Zn-1Mn alloy with different Si additions (0.5, 1, 1.5 wt. % Si) are investigated and morphological changes of Mg-5Sn are observed with the addition of each element like 3Zn and 1Mn. Si added Mg-5Sn-3Zn-1Mn alloy exhibits two different phases namely Mg 2 Sn and Mg 2 Si. Two distinct phases observed are rod like Mg 2 Sn phase and Chinese script Mg 2 Si upto 1wt%. When Si addition exceeds 1.5% polygonal shaped primary Mg 2 Si particles are formed. In Mg-5Sn-3Zn-1Mn alloy addition of Si up to 1wt% enhances the mechanical properties adequately. Above 1 wt% of Si addition, a slight reduction on tensile property is noticed, which is due to the formation of hard, brittle polygonal primary and coarse Chinese script phases.


# 1. Introduction

Automotive industries tend to use light alloys like Aluminium and magnesium which are widely used in vehicle components [1 - 5]. Magnesium alloys are lighter material having higher strength, stiffness attracted widespread interest in improving fuel efficiency and reducing carbon dioxide emissions from vehicles [6 – 12]. Mg-Sn acquired a great interest on the past two decades due to its ability in developing high strength and the need to develop rare earth-free wrought magnesium alloys [13-15]. The solubility limit of Sn in Mg is high at elevated temperature (14.5 wt % at 561 °C) and low on lower temperature, this phenomena makes it suitable for precipitate hardening treatment [17, 18]. Addition of Sn to Mg creates an $Mg_2Sn$ phase that has a melting point of 770°C which affects the mechanical properties of the alloy at higher temperature [18, 19]. Sn is much cheaper than the other RE metals. Mg-Sn based alloys are explored by different researchers with diverse alloy elements such as Zn, Al, Ca, Bi, Y, In, Si, Nd and Mn in different proportions with Mg-Sn binary alloys [17]. Therefore, Mg-Sn based alloys provide ample opportunity in the evolution of high strength and mechanical properties at elevated temperature.

Tin addition to the Mg alloy creates a stable $Mg_2Sn$ compound, which improves its compressive and tensile properties [20]. Mg-Sn alloy shows excellent extrusion capacity when compared with commercially available Mg-Zn and Mg-Al alloys,. This is due to the formation of thermally stable $Mg_2Sn$ phase during hot extrusion rather than the $Mg_{17}Al_{12}$ or $MgZn_2$ phases which have lower melting temperature [21]. Zinc plays an important role in Mg-Sn alloy system, addition of zinc can increase age hardening and mechanical properties due to homogeneously distributed fine $Mg_2Sn$ precipitates. When zinc content in Mg-Sn alloy is increased the strength and ductility also increases at both elevated and room temperature due to the formation of $Mg_2Sn$ and $MgZn_2$ phases [22]. High performance Mg alloys are developed from Mg-Sn-Zn-based alloys [23]. Hence the aim of this study is to understand the impact of Si addition on microstructure and mechanical properties of Mg-5Sn-3Zn-1Mn alloy.

# 2. Experimental Procedure

In this investigation Mg-5Sn, Mg-5Sn-3Zn and Mg-5Sn-3Zn-1Mn alloys are prepared separately in order to evaluate the effect of each alloying element in the Mg-Sn system. Moreover Si addition is varied on Mg-

5Sn-3Zn-1Mn base alloy and its effect is studied. Mg-5Sn-3Zn-1Mn-xSi (x=0.5, 1, 1.5, 2wt %) alloy samples with different wt % of Si are prepared. The composition required is achieved by melting pure Mg, Sn, Zn, Mg-Si and Mg-Mn master alloy in a steel crucible. Melting of metal is carried out in a resistant melting furnace at 750°C. The melting is done in a protective gas atmosphere of 98% Argon and 2% Sulphur hexafluoride to prevent oxidation. Amount of the melt obtained from the crucible is around 3 kg. Skimming is done to remove the slag and the melt is poured into the steel mould at 720°C. The steel mould is preheated to 350°C before pouring in order to avail a defect free cast of dimension 240 x 240 x 30 mm. Samples are machined out precisely from the casted blocks for microstructural analysis by using a wire electric discharge machining WEDM.

Phase analysis is performed by using an x-ray diffractometer (D2Phaser, Bruker, Singapore). The value of absolute intensity for XRD spectra's are normalized by dividing each spectrum value with the highest value to get the values of relative intensity. Specimens for characterization are machined out from the casted alloy as per the standards. Mirror finish microstructural samples are prepared by polishing with different grades of silicon carbide papers, polishing cloth and polishing pastes. Etching is done by using picric acetol based etchant and the microstructure is studied with Olympus optical microscope (Model: BX53MTRF–S, Tokyo, Japan) under different magnification. Advanced characterization is done with the help of scanning electron microscope (JEOL, JSM 35C). Chemical compositions of the phases are determined by using Philips PW1710 powder X-ray energy dispersion spectroscopy (EDS). For each alloy three samples were prepared as per ASTM E8/E8M-09 standards and testing is performed on Instron Universal Testing Machine. Vickers hardness tester (Model: LV700, LECO Corporation, Michigan, U.S.A.) is used for hardness measurement. Hardness measurement is carried out with an indentation load of 5kgf allowing a dwell time of 15 seconds for each indentation.

# 3. Results And Discussion

XRD patterns for alloys Mg-5Sn and Mg-5Sn-3Zn are reported in Fig. 1. XRD analysis result confirms that there is no major impurities or inclusions present in the alloy. Mn addition does not show any significant peaks due to very low percentage of addition. Presence of α-Mg and intermetallics ($Mg_2Sn$) are evident through XRD patterns.

XRD patterns for 0.5 and 2 wt% added Si in Mg-5Sn-3Zn-1Mn alloys is represented in the Fig. 2. Peaks of Diffraction for α-Mg, $Mg_2Sn$ and $Mg_2Si$ compound are detected in the XRD analysis. According to Mg-Si binary diagram, the $Mg_2Si$ phase is formed in the melt during solidification which is confirmed by the results. Moreover, it is noted that with increase of Si content from 0.5 to 2 wt%, the intensity of $Mg_2Si$ peaks increases.

Lower and higher magnification optical microscope results of (a) Mg-5Sn, (b) Mg-5Sn-3Zn and (c) Mg-5Sn-3Zn-1Mn alloys are shown in (Fig. 3). In Mg-Sn binary alloys $Mg_2Sn$ phase exists in the eutectic form (α-Mg+$Mg_2Sn$) shown in the Fig 3a. It is also observed that Mg-Sn alloy possess dendritic structure consisting of gray α-Mg dendritic grain and black secondary phases. The eutectic $Mg_2Sn$ phase is

distributed between α-Mg dendritic arms at grain boundaries. In (Fig.3b) the observed microstructure exhibited coarse dendritic morphology. It also shows the $Mg_2Sn$ phase in the interdendritic region and some of the particles inside the dendrites.

Fig. 3c shows the Mg-5Sn-3Zn alloy in which the dendritic grain size decreases with the addition of Zn. Moreover the interdendritic region is darker and wider compared with the binary Mg-Sn alloy. It shows a phase in the interdendritic region and some of the independent particles are found inside the dendrites. In fig. 3d it is found that the dendritic size is reduced and darker intermetallic is seen. The decrease in the grain size is clearly visible in the microstructure. Chen et al. studied the microstructure of Mg-5Sn-3Zn alloys and observed results of the cast ingot matrix are influenced by dendritic and irregular sediments. Mg-5Sn-3Zn has a rosette shape which is usually a dendritic structure and their interdentritic spacing is relatively large. In fig. 3e with the addition of 1% Mn shows a refined grain structure with $Mg_2Sn$ distributed even and wide on all the grain boundaries. The grain size and amount of dark phase are distributed and the approximate grain size is also gets reduced when compared with Mg-5Sn-3Zn alloy in fig. 3f. This is caused by the addition of Mn which leads to the suppression in the formation of $Mg_2Sn$ and $MgZn_2$ phases.

The microstructure of Mg-5Sn-3Zn-1Mn with different Si additions (0.5, 1, 1.5 and 2 wt %) are shown in fig. 4a-d. An interesting observation was made through the microstructure is the morphology and distribution of $Mg_2Si$ intermetallic. In (Fig. 4a & b) very few $Mg_2Si$ particles are viewed inside the grains and most of them on the grain boundaries. The microstructure of the alloy containing $Mg_2Si$ depends on the amount of Si content; alloys with low-Si content represent the eutectic Chinese script $Mg_2Si$. However, Si content greater than 1.5wt% changes the Chinese script $Mg_2Si$ to polygon type $Mg_2Si$ (Fig. 4c & d) this is clearly visible in higher magnification (fig5d) [24]. The Chinese script shape changes into a polygon and is evenly distributed along the grain boundaries with the increase of Si content. In addition, it was observed that addition of Si did not form another compound with Sn, Zn, or Mn elements.

Figure 5a-d represents the microstructural results of higher magnification to reveal the Chinese script and Polygon shapes of $Mg_2Si$ discussed in the context above. Guangyin et al. [25] studied the morphology of the microstructure of Mg-6Zn alloy with the addition of Si.

Microstructure results indicate the presence of interdendritic MgZn and Chinese-script $Mg_2Si$ particles in Mg matrix. Karakulak 2018 et al. [17] examined the morphological changes of the Mg-5Sn and Mg-10Sn binary alloys by adding Si. The examined microstructure revealed that addition of silicon to the binary alloy increase the amount of intermetallics at the grain boundary.

**Table 1.** EDS result for Mg-5Sn-3Zn-1Mn alloy

| Element | MgK | | SnL | | ZnK | | MnK | |
|---|---|---|---|---|---|---|---|---|
| | wt% | at% | wt% | at% | wt% | at% | wt% | at% |
| A | 10.92 | 89.68 | 4.42 | 7.43 | 0.85 | 2.58 | 0.09 | 0.31 |
| B | 5.05 | 73.60 | 7.96 | 23.73 | - | - | 0.49 | 2.67 |
| C | 16.11 | 98.49 | 0.57 | 0.71 | 0.18 | 0.41 | 0.15 | 0.4 |

Fig. 6 shows the SEM-EDS analysis of Mg-5Sn-3Zn-1Mn alloy for analysing phases and the energy diagram of different region are shown in figure 7. The EDX energy values are tabulated in table 1. SEM-EDX results provide the presence of second phase which is a rod-shaped $Mg_2Sn$ on the grain boundary. Area analysis of region A displays the presence of the maximum elements like Mg, Sn, Zn and trace element like Mn. Solid solution mixtures of all the added elements are tabulated in table 1. Region B indicates the point analysis of SEM micrograph which shows that the white region consists of the interdendritic is $Mg_2Sn$ phases and similar findings are also observed by Zhang et al. [26]. Area analysis of region C indicates the maximum of Mg i.e., 98at% in the EDS analysis and minimum amount of other elements such as Sn, Zn and Mn. This confirms that this dendritic region is a solid solution of α-Mg matrix.

Fig.8 shows the SEM micrograph of Mg-5Sn-3Zn-1Mn-2Si alloy. In the α-Mg matrix there are two basic types of secondary phases are observed. The SEM-EDS results show the detail of $Mg_2Sn$ and $Mg_2Si$ secondary phases. $Mg_2Sn$ as rod-shaped in the interdendritic region and $Mg_2Si$ are like Chinese script and polygonal structure. Upto 1wt% of Si Chinese script $Mg_2Si$ structure and above 1.5wt% fine polygonal structure is observed from the EDX analysis.

**Table 2** EDS result for Mg-5Sn-3Zn-1Mn-2Si alloy

| Element | MgK | | SnL | | ZnK | | MnK | | SiK | |
|---|---|---|---|---|---|---|---|---|---|---|
| | wt% | at% | wt% | at% | wt% | at% | wt% | at% | wt% | at% |
| A | 3.42 | 95.27 | 0.4 | 2.3 | 0.23 | 2.43 | - | - | - | - |
| B | 1.42 | 65.52 | 3.01 | 28.39 | - | - | - | - | 0.15 | 6.08 |
| C | 2.38 | 61.20 | 0.35 | 1.85 | - | - | 0.01 | 0.12 | 1.66 | 36.83 |
| D | 2.32 | 82.85 | - | - | - | - | - | - | 0.55 | 17.15 |

EDX energy diagram of different region are shown in fig. 9. Region A shows the point analysis, which indicates the presence of Mg, Sn and Zn elements around the grain boundary. The amount of elements

present in the region is shown in the Table 2. The point analysis of white region B indicates the presence of $Mg_2Sn$ phase. The area EDS analysis of region C primarily indicates the presence of Mg and Si elements and it confirms $Mg_2Si$ phase which is tabulated. According to the EDS analysis, the Chinese script structure shows the composition of $Mg_2Si$ (region D).

The system has a eutectic temperature of 637°C based on the phase diagram of Mg-Si and the precipitation temperature of $Mg_2Si$ is higher than other intermetallics like $Mg_2Sn$ and $MgZn_2$. It is almost impossible for these above mentioned particles to act as a heterogeneous site for nucleation on the phase of $Mg_2Si$ as prepared in different literatures [26, 27]. This argument is consistent with the results obtained in the paper. It is inferred from the fig. 8 region C has bright particles formed around the gray $Mg_2Si$ particles. EDS analysis reports that an irregular reticular arrangement at the boundary of grains having rod-shaped $Mg_2Sn$ particles. When comparing Mg-5Sn-3Zn-1Mn, with Si addition, the Chinese script phase of $Mg_2Si$ is located within the grain and grain boundaries, and with the addition of Si, its fraction of volume increases [22].

### 3.1 Hardness

Fig.10 depicts the Vicker's hardness values for the cast base alloy and different Si added Mg-5Sn-3Zn-1Mn alloys. It is observed from the figure that with increasing Si content, the hardness is increased from 36 to 44 Hv. This enhancement in hardness of the alloy is due to the presence of hard $Mg_2Si$ intermetallic phase with increase in the Si addition. Moreover, increasing volume of $Mg_2Si$ with Si addition increases hardness. Addition of Si to the binary alloy reduces the size of the alloy grains and increases the hardness. Similar results have been reported by Vignesh. P et al. [20].

Comparing with the base alloys (Mg-5Sn, Mg-5Sn-3Zn and Mg-5Sn-3Zn-1Mn) Si added alloys show increased hardness value. Comparing with hypoeutectic (i.e., 0.5 and 1 wt% Si) alloys, the hypereutectic (i.e., 1.5 and 2 wt% Si) alloys have higher hardness which is due to the presence of the hard brittle polygonal primary $Mg_2Si$ crystals in the matrix along with the Chinese script eutectic.

### 3.2 Tensile Properties

Figure 11 shows the values of the ultimate tensile strength (UTS) and yield strength (YS) of the various Si added alloys. The values of UTS and YS increase by up to 1% Si addition after which the values begin to decrease. However, the UTS and YS values of 2 wt% Si added alloys are greatly reduced. The overall observation from this study shows that 0.5 and 1 wt% of Si provides better tensile properties. The increase in UTS and YS in 0.5 and 1 wt% alloy leads to increase in the eutectic volume. The reduction in the strength properties beyond 1.5 wt% is due to the existence of high volume of coarse Chinese script and brittle polygonal primary $Mg_2Si$ phases in the alloy.

The as cast alloys mechanical properties are determined by the intermetallic distributions and its morphology. Chen et al. [22] reported that on matrix $Mg_2Sn$ and MgSnY compounds are widely

distributed. Mechanical properties are integrated while there are tiny rod-like deposits ($MgZn_{2n}$ and $Mg_2Sn$), the strength and ductility increases and with the presence of huge, asymmetrical MgSnY clusters, elongation is greatly reduced. When the $MgZn_2$ nucleation is stimulated by $Mg_2Sn$, precipitates of fine size (2 - 4 μm) are present at the boundaries of grains and within the grains, the grain boundaries are stabilized in deformation due to fine phases and properties of cast alloy is provided by the precipitates. In addition, dissociation loops form and the dislocation loop moves towards the precipitates. $MgZn_2$ particles stimulated by $Mg_2Sn$ are useful in dislocation tangle and improving strength [6, 22]. Similar interpretations are formed in the present study also.

The improvement in tensile strength was mainly due to two aspects: (1) refinement of the microstructure and (2) formation of precipitates like $Mg_2Sn$ & $Mg_2Si$. Above 1.5wt% of Si the reduction of mechanical properties are due to the changes of $Mg_2Si$ morphology. Along interfaces long crack easily nucleates between Chinese script $Mg_2Si$ particle and the Mg matrix. Similarly Guangyin et al. [25] Kumar et al. [28] reported with an increase of 0.25% calcium, the tensile strength decreases. Too much calcium addition enhances the quantity of coarse polygonal $Mg_2Si$ particles that has negative outcome on mechanical properties. Fracture surfaces of the tested specimens are shown in the figure 12. In the fractographs it is observed that addition of Si increases brittleness (cleavages) and occurrence of secondary cracks. This implies that the coarse particles initiate sites for fracture. Shallow dimples in the fractograph reveal shear deformation [29].

# 4. Conclusion

1. Si addition to Mg-5Sn-3Zn-1Mn alloy results in the formation $Mg_2Sn$ and $Mg_2Si$ precipitates. The morphology of each phase is different. $Mg_2Sn$ phase is rod like phases and the $Mg_2Si$ shows Chinese script structure upto 1wt% of Si. Above 1.5% Si addition shows polygonal shaped particles.
2. The mechanical properties of the Mg-5Sn-3Zn-1Mn alloy are enhanced with the Si addition, up to 1 wt%. Reason for the improvement in tensile strength is due to two aspects: (1) microstructural refinement and (2) precipitate formation of $Mg_2Sn$ & $Mg_2Si$. The reduction of mechanical properties above 1.5wt% of Si is due to the brittle polygonal $Mg_2Si$ morphology.

# 5. Declarations

**Acknowledgements** The Authors wish to thank the casting and characterization facilities provided by MatRICS – Materials Research and Innovation Centric Solutions, Vellimalai, Kanyakumari District, India, Tel: **+**91 91766 06699; web: www.matrictech.com.

**Funding:** No funds, grants, or other support was received.

**Conflicts of interest:** The authors declare that they have no conflicts of interest.

**Availability of data and material:** All the original data are available with the corresponding author.

**Compliance with Ethical Standards:**

**Code availability:** Not applicable.

**Consent for publication:** Open choice.

# 6. References


1. Azadi M (2017) J. Fatigue. 99: 303-314.
2. Diqing W, Houbin W, Jiajun H, Yinglin H, Linsen W, Kangjin F (2019) Mater. Int. https://doi.org/10.1007/s12540-019-00477-y.
3. Kim D.H.L.S.H, Kim H.J, Moon B.G, Kim Y. M, Park S. H (2020) Mater. Int. https://doi.org/10.1007/s12540-020-00867-7.
4. Ramalingam V.V, Ramasamy P, Kovukkal M.D, Myilsamy G (2020) Mater. Int., 26:409-430.
5. Jin X, Xu W, Shan D, Liu C, Zhang Q (2017) Mater. Int. 23:434-443.
6. Wang Y, Peng J, Zhong L (2018) Alloy. Compd. 744:234-242.
7. Maleki E, Shahri F, Emamy M (2019) Mater. Int. https://doi.org/10.1007/s12540-019-00530-w.
8. Suh J.S, Suh B.C, Choi J.O, Kim Y.M., You B.S (2020) Mater. Int. https://doi.org/10.1007/s12540-020-00642-8.
9. Park M, Okayasu K, Fukutomi H, Kim K (2016) Mater. Int., 22:1129-1132.
10. Park S.S, Park Y.S, Kim N.J, (2002) Met. Mater. Int., 8: 551-554.
11. Lee C.D (2002) Met. Mater. Int. 8:283-288.
12. Sivapragash M, Kumaradhas P, Retnam B.S.J, Joseph X. F, Pillai U.T.S (2016) Mater. Des. 90**:**713–722
13. Suneesh E, Sivapragash M (2019) Rare Met. https://doi.org/10.1007/s12598-019-01281-8
14. Durai T. J, Sivapragash M, Vettivel S. C, Aurtherson P.B (2020) Met Sci Heat Treat+, 62:285 – 291
15. Liu C.Q, He C, Chen H.W., Nie J.F (2020) J. Mater. Sci. Technol. 45:230–240.
16. Wang Y, Peng J, Zhong L, (2018) J. Alloys Compd. 744:234-242.
17. Karakulak E, Kucuker Y.B (2018) J. Magnes. Alloys 000:1–6
18. Hu T, Xiao W, Wang F, Li Y, Lyu S, Zheng R, Ma C, (2018) J. Alloy. Compd. 735:494-1504.
19. Sun Z, Li Y, Zhang K, Li X, Ma M, Shi G and Yuan J (2020) Mater. Lett. 276:128214.
20. Vignesh P, Venkatesh G .S. Kumaran, Mater. Today **27** 2445-2448, (2020).
21. Kim S.H and Park S.H, (2018) Mat. Sci. & Eng. A 733:285–290.
22. Chen Y, Wang Y, Gao J, (2018) J. Alloy. Compd. 740:727-734.
23. Chai Y, Jiang B, Song J, Wang Q, Gao H, Liu B, Huang G, D. Zhang, F. Pan (2019) J. Alloy. Compd. 782:1076-1086.
24. Hamu G.B, Eliezer D, Shin K.S., (2008) Intermetallics, 16:860-867.

25. Guangyin Y, Manping L, Wenjiang D, Inoue A (2003) Sci. Eng. A. 357:314-320.
26. Zhang T, Cui H. X.Cui, Zhao E, Pan Y, Feng R,.Jia Q, Zhao J (2019) J. Alloys Compd. 784:1130-1138.
27. Alizadeh R, Mahmudi R., J (2011) Alloys Compd. 509:9195-9199
28. Kumar K.K.A, Pillai U.T.S, Pai B.C, Chakraborty M (2013) Met. Mater. Int. 19: 1167-1172.
29. Poddar P, Kamaraj A, Murugesan A.P, Bagui S, Sahoo K.L (2017) J. Magnes. Alloys 5:348–354.

# Figures

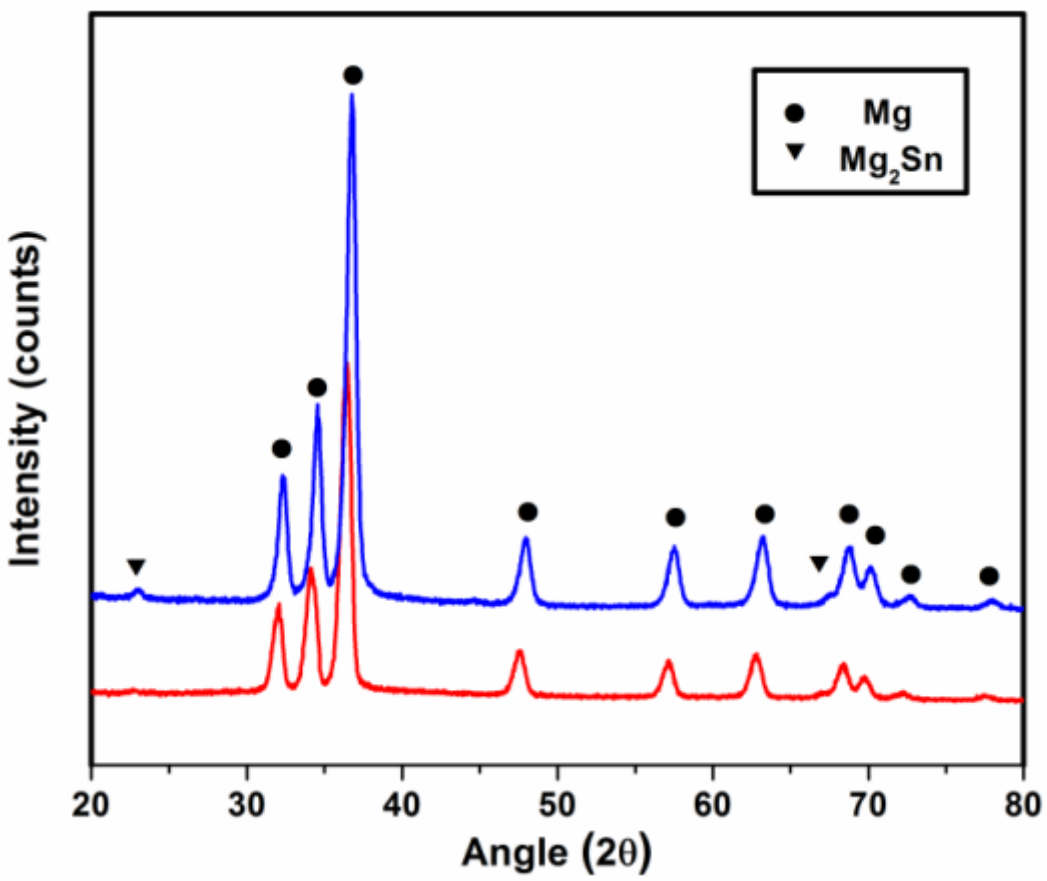


**Figure 1**

XRD patterns of Mg-5Sn and Mg-5Sn-3Zn

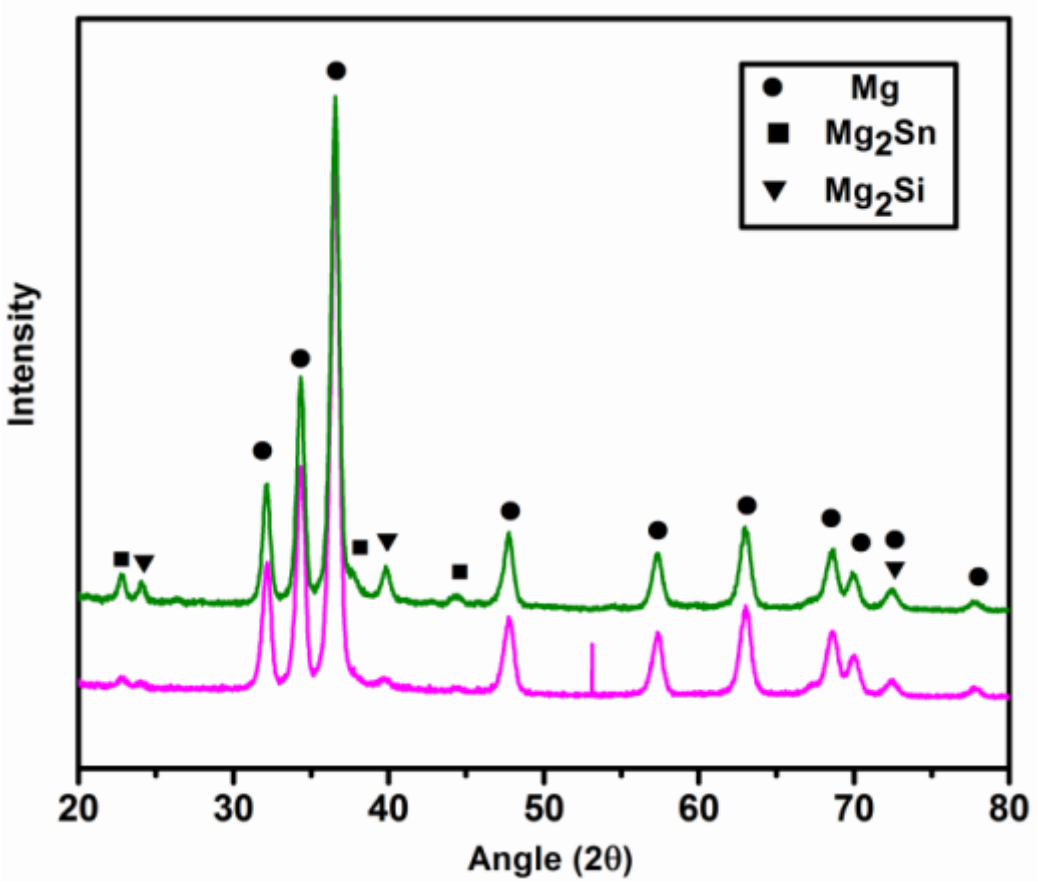


**Figure 2**

XRD patterns of Mg-5Sn-3Zn-1Mn-0.5Si and Mg-5Sn-3Zn-1Mn-2Si alloys.

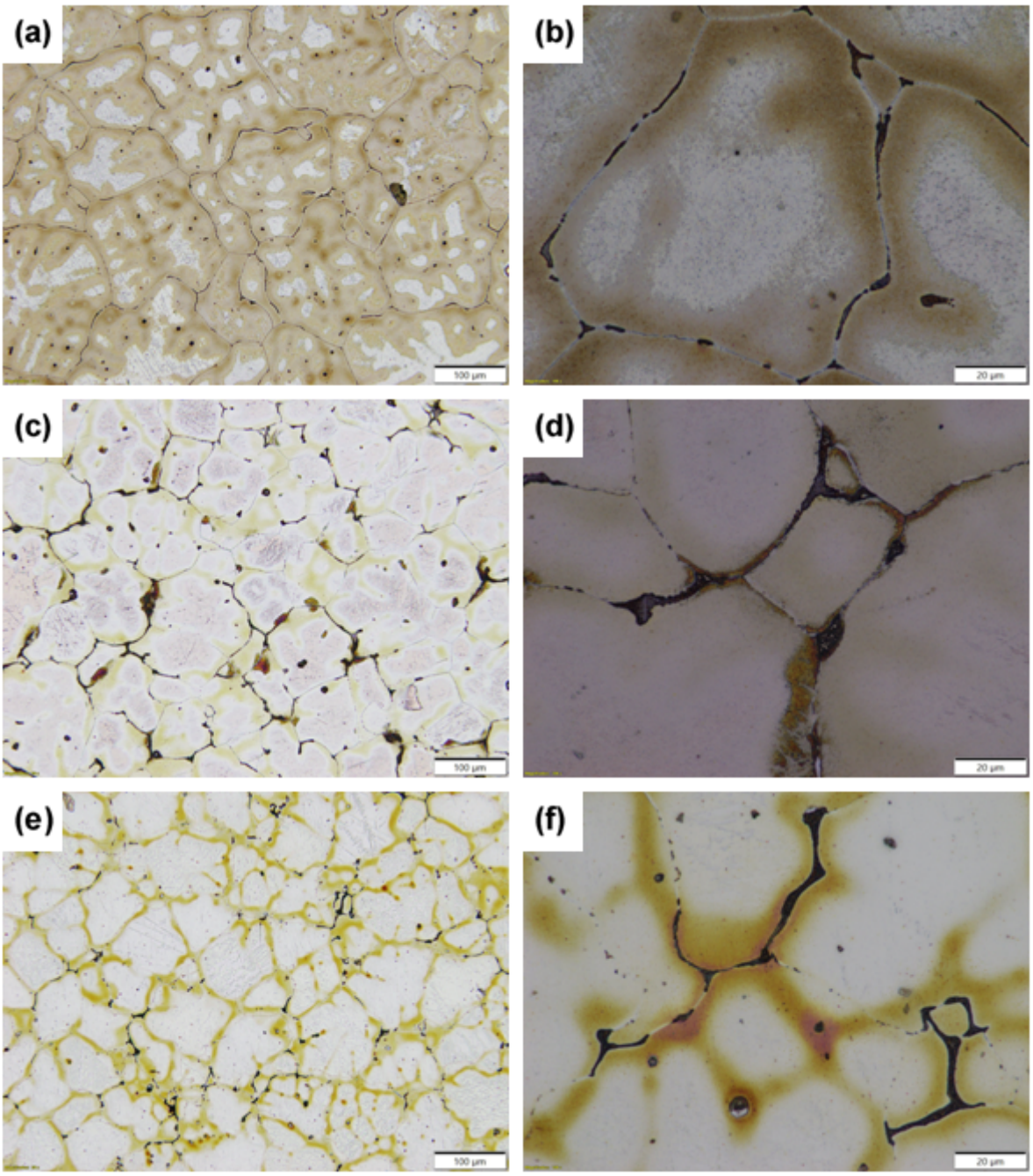


## Figure 3

Lower and higher magnification optical microstructure results: (i) Mg-5Sn (a, b); (ii) Mg-5Sn-3Zn (c. d); (iii) Mg-5Sn-3Zn-1Mn (e, f).

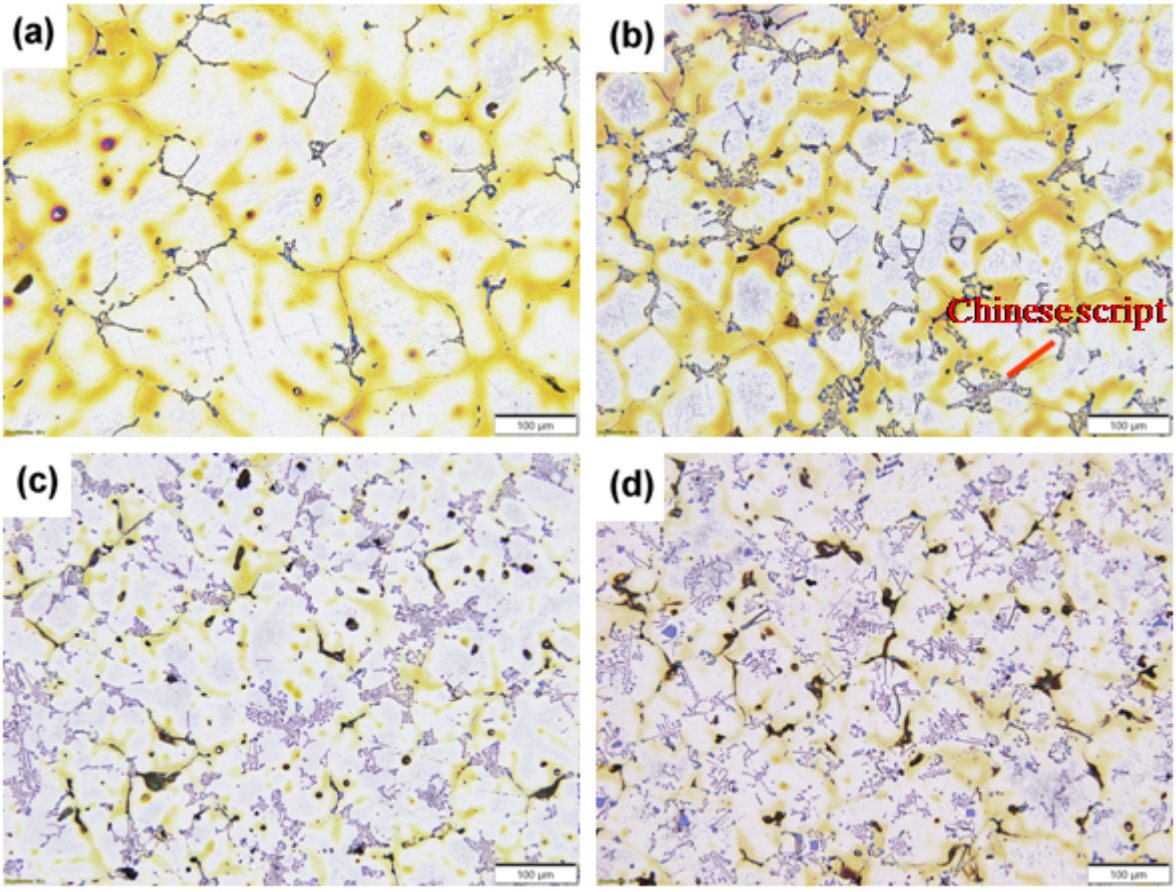


## Figure 4

Optical microstructure of Mg-5Sn-3Zn-1Mn-xSi alloy (a) 0.5% Si, (b) 1% Si, (c) 1.5% Si and (d) 2% Si

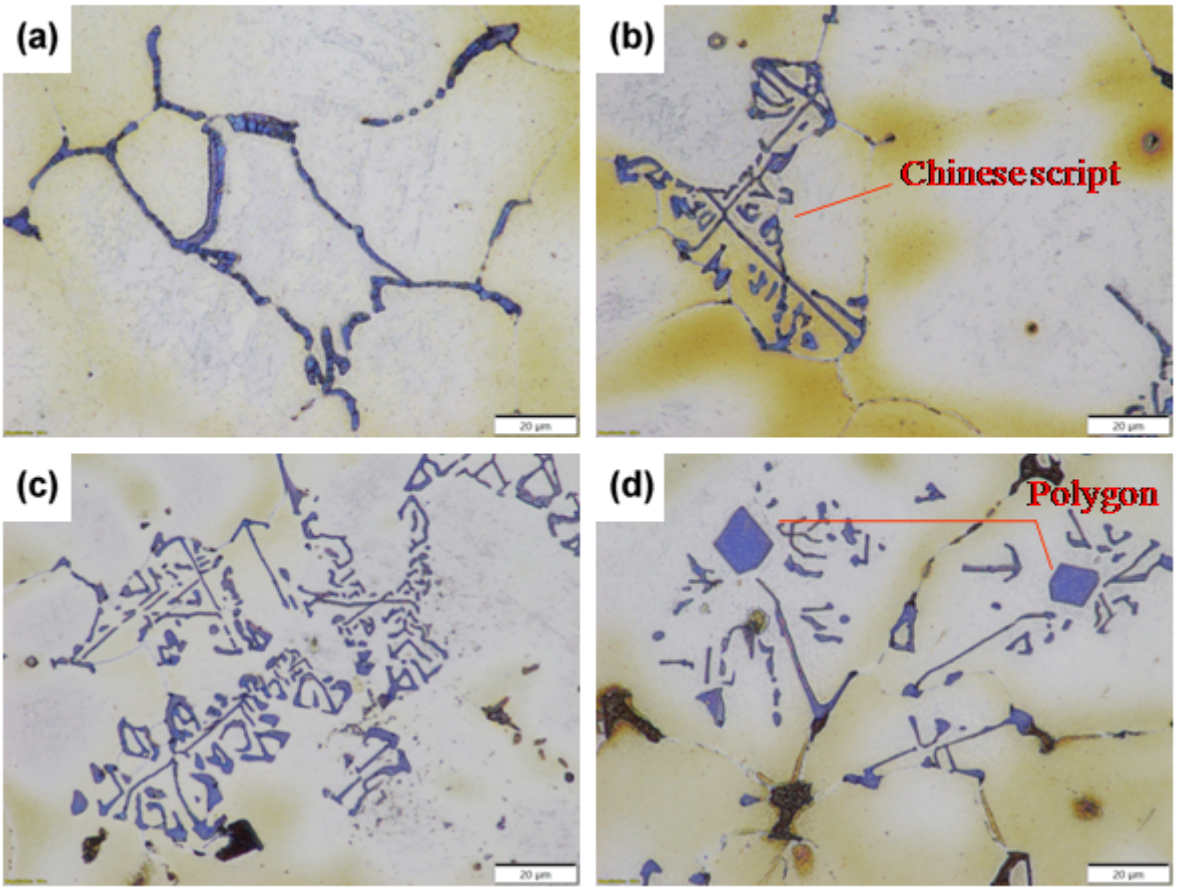


**Figure 5**

High magnification optical microstructure of different Si added Mg-5Sn-3Zn-1Mn-xSi alloy (a) 0.5% Si, (b) 1% Si, (c) 1.5% Si and (d) 2% Si

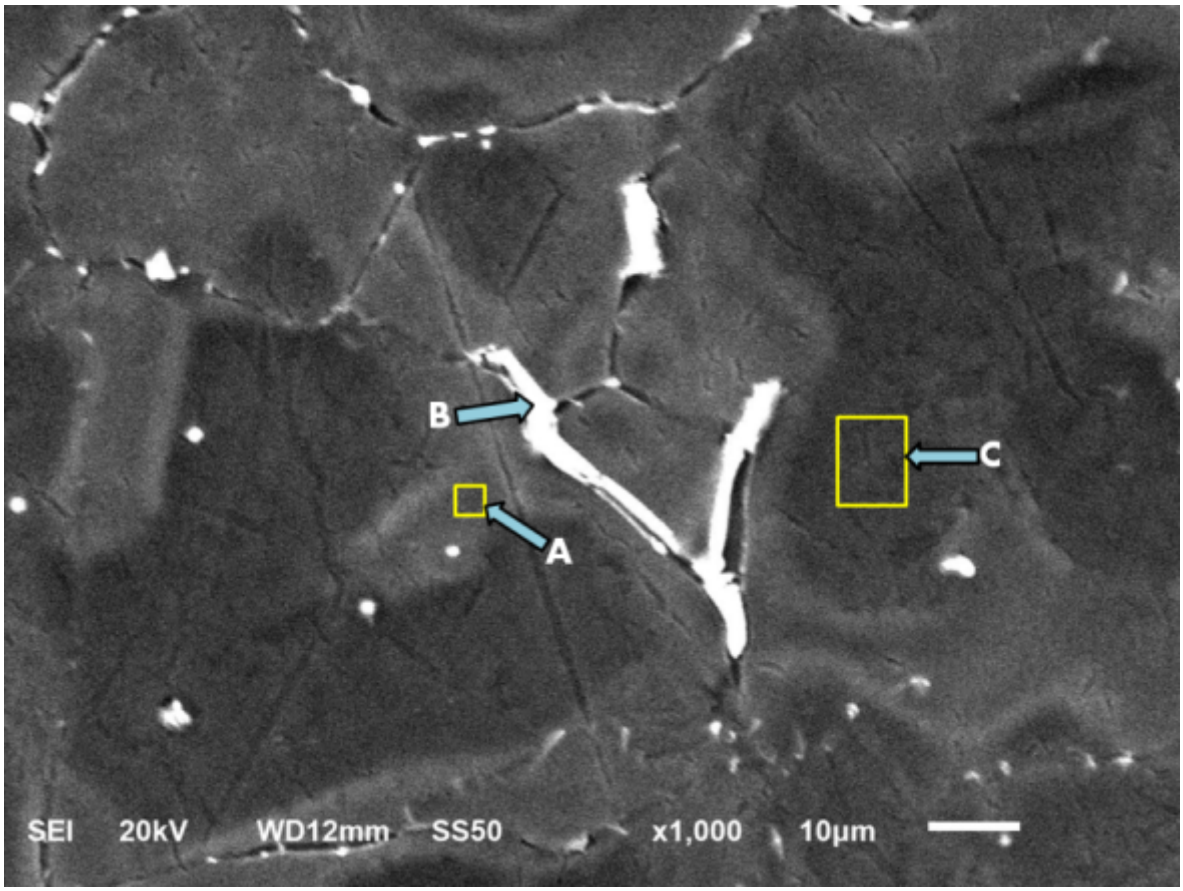


## Figure 6

The high magnification SEM micrographs of Mg-5Sn-3Zn-1Mn alloy

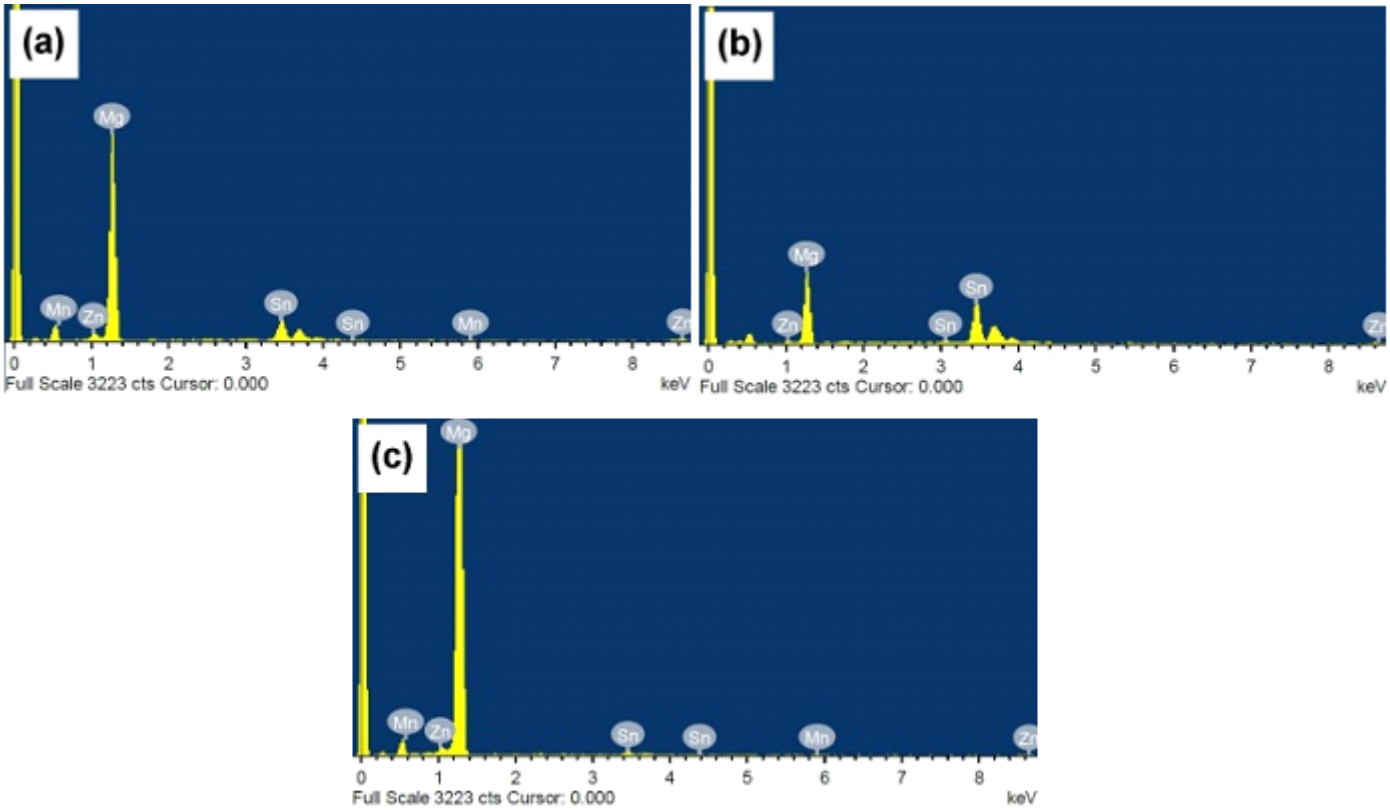


## Figure 7

EDX micro analysis for SEM micrographs (a) at A, (b) at B and (c) at C

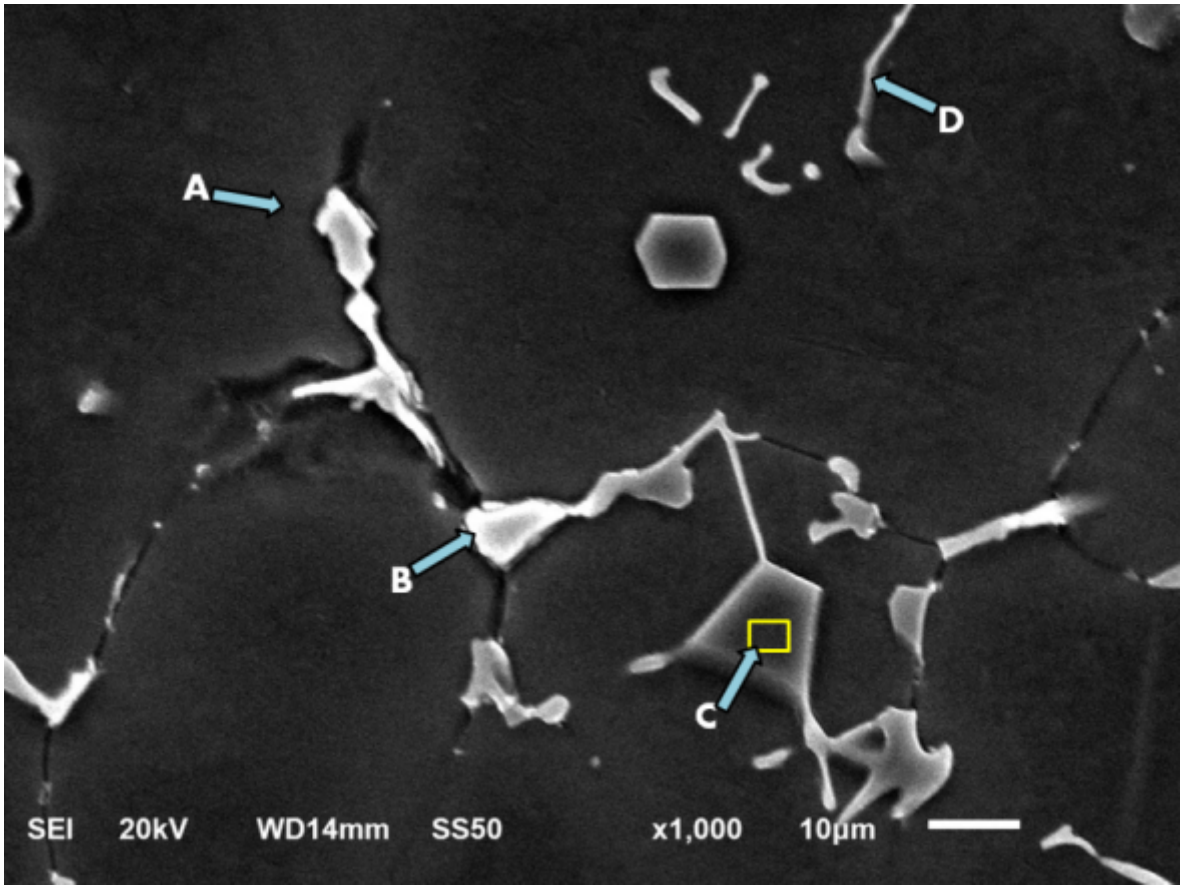


## Figure 8

The high magnification SEM micrographs ofMg-5Sn-3Zn-1Mn-2Si alloy

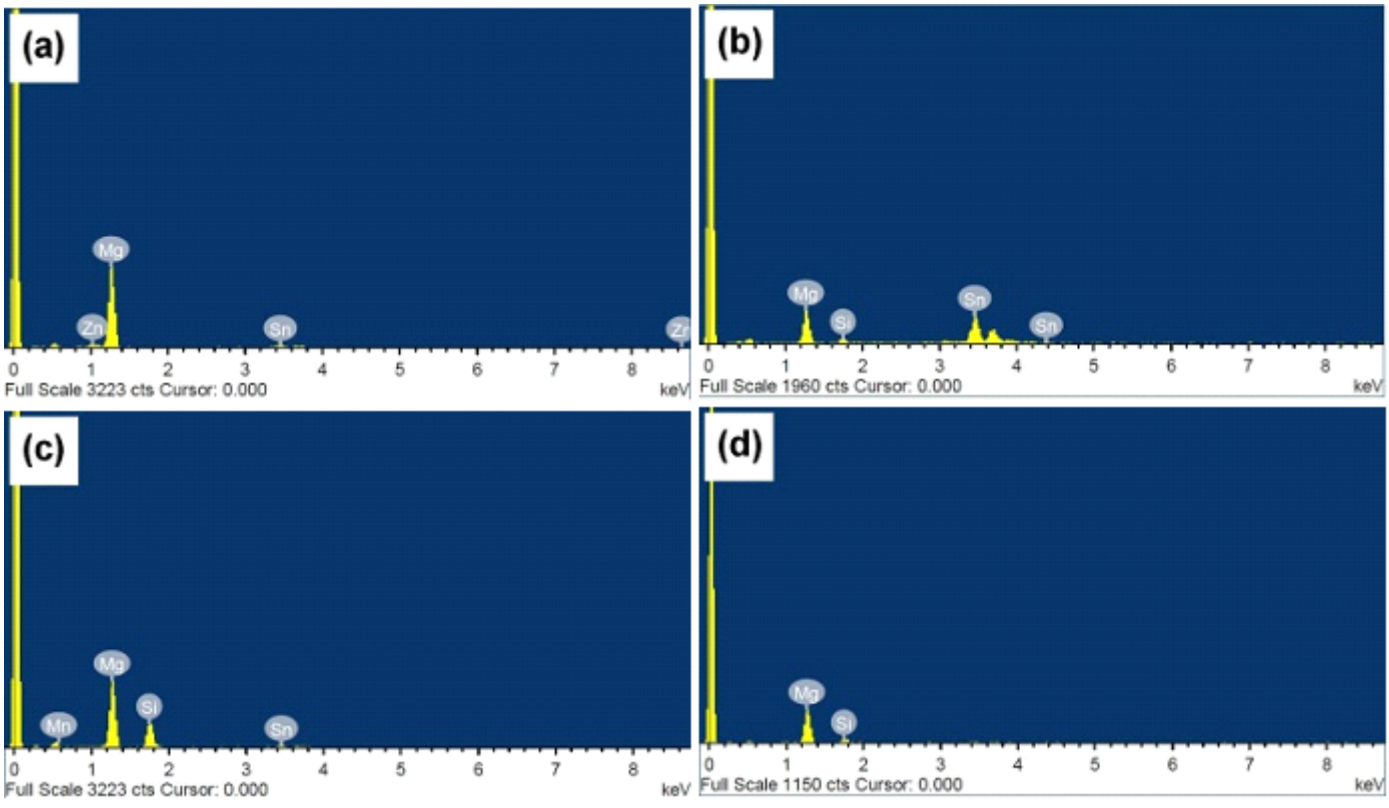

## Figure 9

EDX micro analysis for SEM micrographs (a) at A, (b) at B, (c) at C and (d) at D

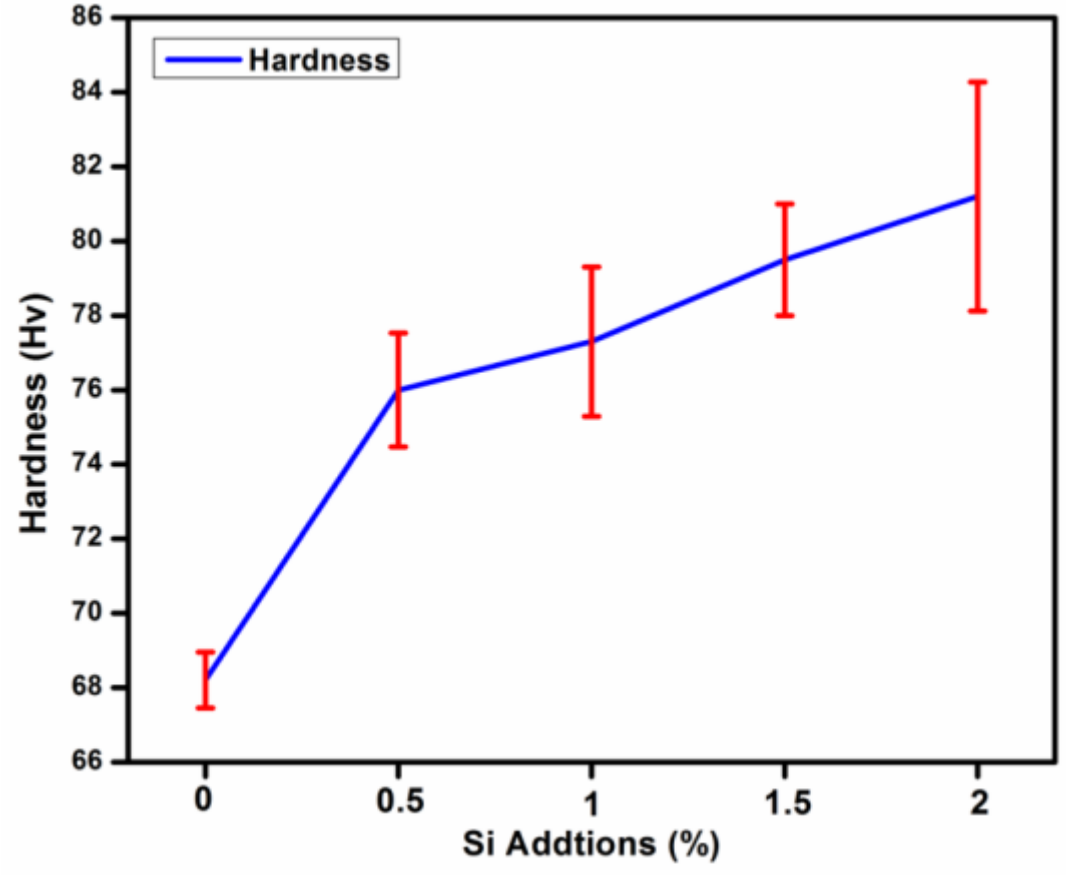


## Figure 10

Hardness of Mg-5Sn-3Zn-1Mn alloy with varied %Si content

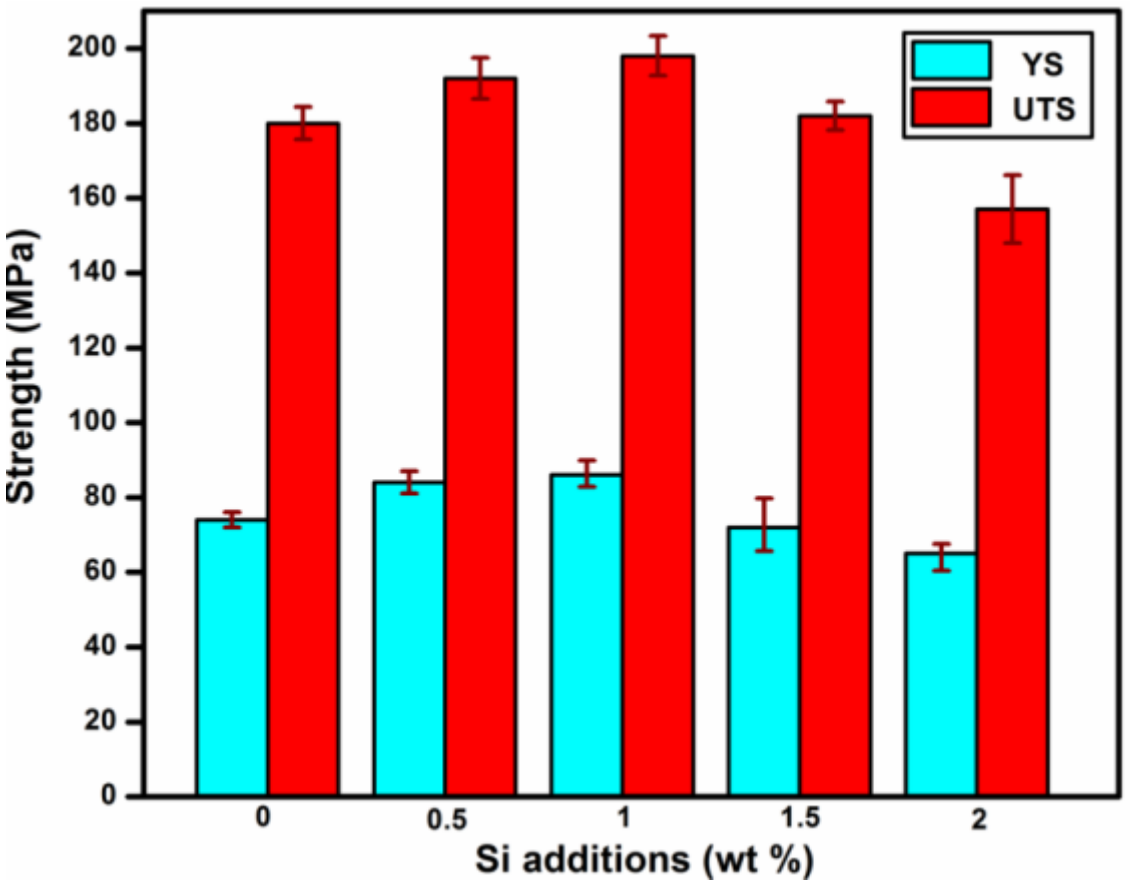


**Figure 11**

Tensile properties of Mg-5Sn-3Zn-1Mn with different Si additions

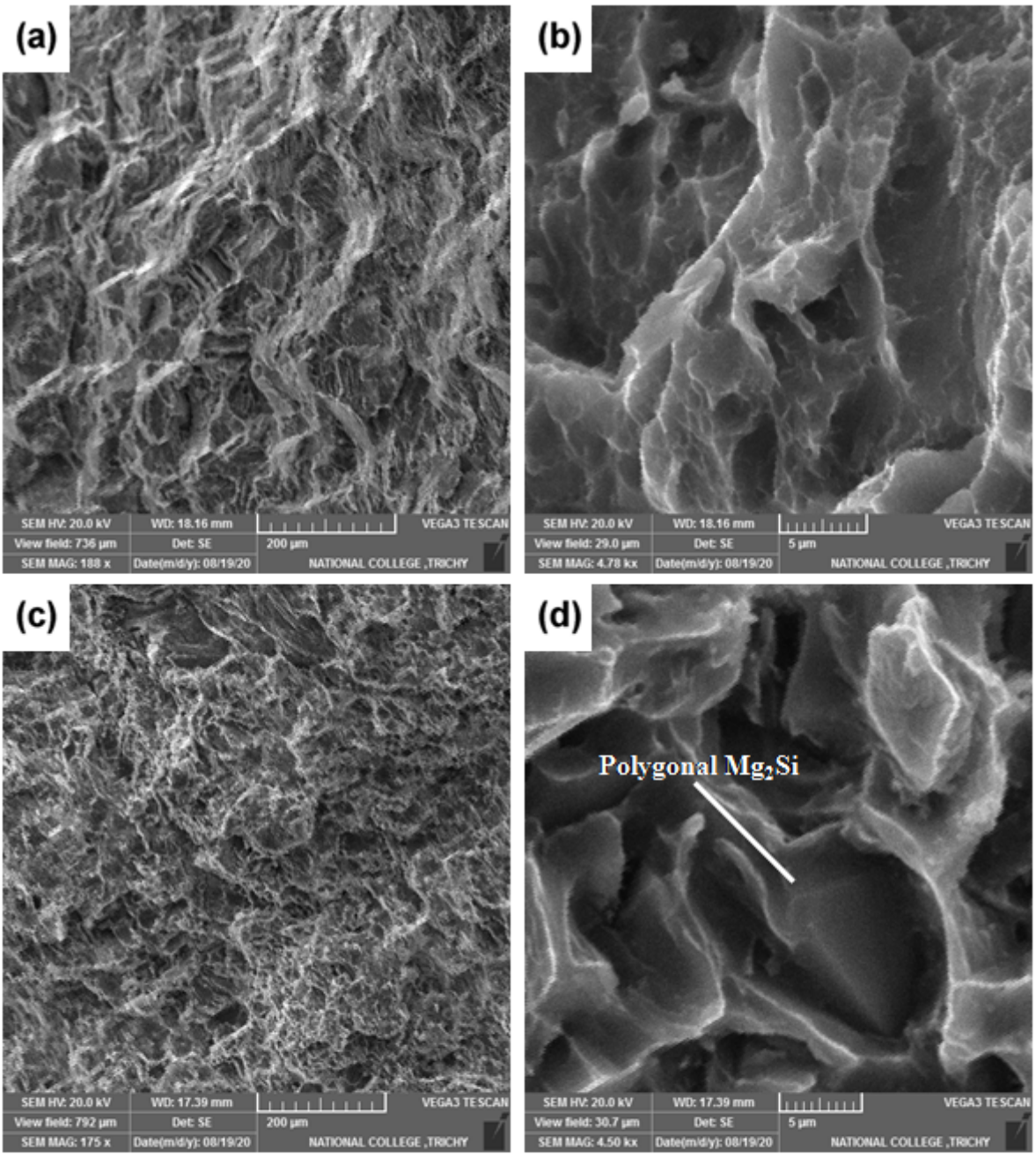


## Figure 12

Lower and higher magnification SEM fractograph (i) Mg-5Sn-3Zn-1Mn base alloy (a,b); (ii) Mg-5Sn-3Zn-1Mn-2Si alloy (c,d)